# Higher-dimensional Euclidean and non-Euclidean structures in planar circuit quantum electrodynamics

Alberto Saa [*]
*Department of Applied Mathematics, University of Campinas (UNICAMP), 13083-859 Campinas, São Paulo, Brazil*

Eduardo Miranda [†] and Francisco Rouxinol [‡]
*Institute of Physics Gleb Wataghin, University of Campinas (UNICAMP), 13083-859 Campinas, São Paulo, Brazil*

(Received 25 August 2021; revised 11 August 2025; accepted 9 December 2025; published 5 January 2026)

We demonstrate that a recent proposal for simulating planar hyperbolic lattices using circuit quantum electrodynamics can be extended to include higher-dimensional lattices in both Euclidean and non-Euclidean spaces by allowing circuits that involve more than three polygons at each vertex. The quantum dynamics of these circuits, which we are developing with current technology, are governed by effective tight-binding Hamiltonians that correspond to higher-dimensional Kagomé-like structures (such as $n$-dimensional zeolites). These structures are known for exhibiting strong frustration and flat bands. We analyze the spectra of both hyperbolic and positive-curvature lattices and derive exact expressions for the fraction of flat-band states. Our findings significantly broaden the possibilities for realizing non-Euclidean geometries using circuit quantum electrodynamics, a research direction we are actively pursuing in microwave-guide circuits constructed with sputtered niobium films on silicon substrates.

DOI: 10.1103/z2zk-m4c3

## I. INTRODUCTION

There has been a long history of cross-pollination between geometry and various areas of physics [1]. Geometry is at the base of general relativity and cosmology, leading also to surprising semiclassical effects such as Hawking radiation. The difficulty of directly observing these subtle quantum effects in a gravitational context has spurred the search for analogs in condensed-matter systems [2–6]. Nonflat geometries, however, have proven fruitful even in situations that are not gravity related. A prime example is geometric frustration. The optimal *local* packing of hard spheres in an icosahedral structure cannot be periodically extended in Euclidean space. It is, however, compatible with periodicity in hyperbolic space, which can then serve as a starting point. The real system can then be approximated and analyzed by introducing defects into the pristine hyperbolic idealization (see, e.g., Ref. [7] for a review). Other examples of this cross fertilization include the control of infrared singularities in classical and quantum field theories in hyperbolic space [8], the anti–de Sitter/conformal field-theory duality [9], phase transitions in curved spaces [10–12], and hyperbolic surface codes for quantum computation [13], among many others.

More recently, the flexibility of the design of circuit quantum electrodynamics (cQED) [14–16] has enabled the experimental realization of hyperbolic lattices using planar microwave circuits [17–19]. In these systems, multiple microwave resonators are capacitively coupled to form an artificial photonic lattice. The photon dynamics can be effectively described by a tight-binding model in a hyperbolic plane. This important achievement has stimulated some recent advances such as the formulation of a band theory in hyperbolic lattices [20] or proposals for the realization of topological phases [21].

A promising direction that follows from these results is the integration of superconducting qubits into these architectures, allowing for the implementation of fully interacting models [22,23]. As far as we know, however, such experiments have not yet been reported for either the $q = 3$ or $q > 3$ cases. Although there are reports describing measurements involving $N = 3$ sites with qubits in a Ph.D. thesis [24], no peer-reviewed publications have resulted from those results. Other recent works [25–27] explore lattices with superconducting qubits, but in distinct network topologies.

A severe limitation of the systems built so far is their confinement to strictly two-dimensional lattices. Indeed, the planar layout of the circuits seems, at first, to preclude a higher-dimensional setup. We propose in this paper a way to overcome this limitation by increasing the connectivity of the microwave resonators. This is achieved by means of a capacitive coupling design that can symmetrically couple $q > 3$ resonators with equal strength, a $q$-leg capacitor that can be easily constructed with present technology (see Fig. 1). As a result, even though the device layout is contained within the usual planar design, the effective dimension of the underlying dynamics is greater than 2, forming a so-called $n$-zeolite framework [28]. This enlarges considerably the range of possible applications and opens the possibility of exploring different hyperbolic structures with flat bands, as we will show. It also affords the flexibility of generating a spatially varying connectivity and, consequently, a nonhomogeneous geometric configuration. Besides exploring this new design in both cases of positive and negative curvature, we also derive some results regarding the spectra of these systems, such as

[*]Contact author: asaa@ime.unicamp.br
[†]Contact author: emiranda@ifi.unicamp.br
[‡]Contact author: rouxinol@ifi.unicamp.br

 

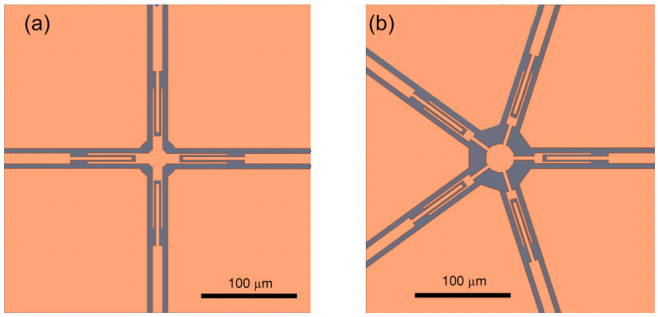


FIG. 1. Proposed planar $q$-leg capacitive devices coupling the resonators for (a) $q = 4$ and (b) $q = 5$. We are building these circuits using standard microfabrication techniques. In the 4-leg capacitor (a), for instance, the capacitance between any pair of legs is 374 pF, with deviations smaller than 0.01 pF. The generic case with $q$ symmetrical legs follows analogously as a star-shaped configuration with $q$ leaves. See the Appendix A further construction details.

a generic expression for the fraction of flat-band states and some bounds for the largest eigenvalues of full and half-wave modes.

In the following section, we will provide a brief review of some fundamental results in circuit quantum electrodynamics (cQED), including their layouts and the underlying lattices. Section III will focus on higher-dimensional geometries and the circuits associated with them. Our main results will be presented in Sec. IV, while the final remarks will be discussed in Sec. V. Some construction details for the $q$-leg capacitor are included in Appendix A.

## II. SUPERCONDUCTING CIRCUITS AND LATTICES

Let us briefly review some of the basics of cQED [17–19]. These photonic systems consist of identical quantum microwave resonators disposed along the edges of a layout lattice. Each vertex of the lattice is a $q$-leg capacitor, responsible for the symmetric pairwise coupling between the $q$ resonators meeting at that vertex. This defines a lattice called the layout graph $G$ [see Figs. 2(a) and 2(c)]. The underlying quantum dynamics of the system is governed by a tight-binding Hamiltonian

$$H = H_0 + H_I = \omega_0 \sum_i a_i^\dagger a_i - \sum_{\langle i,j \rangle} t_{ij}(a_i^\dagger a_j + a_j^\dagger a_i), \qquad (1)$$

where $\omega_0$ is the resonator frequency. The off-diagonal term $H_I$ describes the hopping (with amplitude $t_{ij}$) of photons between resonators induced by the capacitors. It is clear that the sites of the Hamiltonian of Eq. (1) should be taken to be the midpoints of the edges of the layout lattice, and its connectivity is determined by the capacitors. This underlying lattice is called the line graph, which we will denote by $L(G)$ [see Figs. 2(b) and 2(d)].

In order to describe either type of graph we will use Schläfli's $\{p, q\}$ notation for two-dimensional regular tilings. It denotes a tiling with $p$-regular polygons, or $p$-gons, disposed so that $q$ of them meet at every corner. A regular hyperbolic tiling requires only

$$\tau = (p-2)(q-2) > 4, \qquad (2)$$

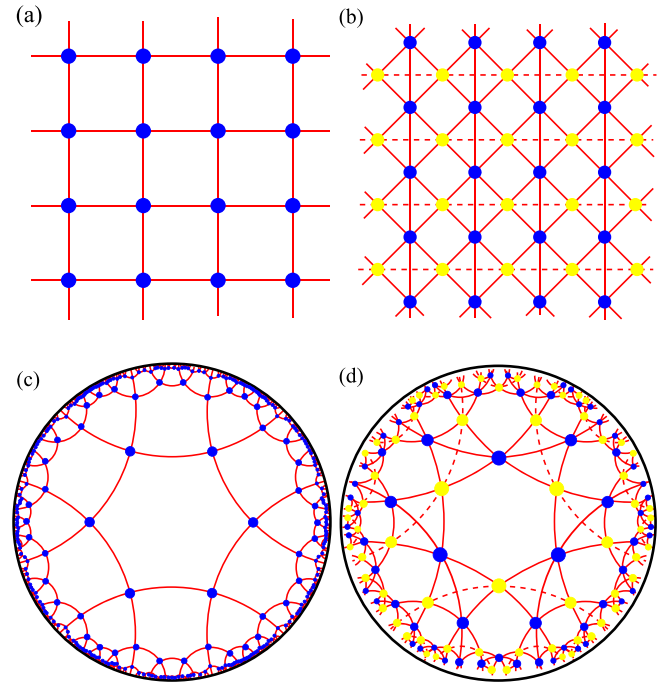


FIG. 2. Some examples of tilings with $q = 4$ and their associated line graphs. (a) The usual square $\{4, 4\}$ tiling of $\mathbb{E}^2$ and (b) its associated line graph, which is equivalent to a single layer of corner-sharing tetrahedra (3 zeolites) in $\mathbb{E}^3$, with the blue and yellow vertices located in two parallel planes and seen from a perpendicular viewpoint. (c) The hexagonal $\{6, 4\}$ tiling of $\mathbb{H}^2$ and (d) its associated line graph, which can be viewed in an analogous way: a single layer of corner-sharing tetrahedra in $\mathbb{H}^3$ (or in $\mathbb{H}^2 \times \mathbb{R}$), viewed from above. Note that a layered geometrical realization of the line graphs of (b) and (d) are only available for $\{p, 4\}$ tilings with even $p$, since the disposition of the blue and yellow vertices in two parallel planes is only possible if the line graph is bipartite. We employ here Schläfli's $\{p, q\}$ notation for two-dimensional regular tilings (see text).

with no further restrictions on the polygons besides being convex and regular. Hence, there are (countably) infinitely many regular tilings of the hyperbolic plane $\mathbb{H}^2$, in contrast to the possible tilings of the usual Euclidean plane $\mathbb{E}^2$ and the sphere $\mathbb{S}^2$, for which $\tau = 4$ and $\tau < 4$, respectively. The particular choice of $q = 3$ for the layouts explored in Ref. [17] leads to line graphs that are Kagomé lattices of corner-sharing triangles. These are highly frustrated two-dimensional lattices with characteristic flat bands in their tight-binding spectra [17–19].

The absolute value of $t_{ij}$ is homogeneous in the lattice, but its sign may vary. Two sets of modes arise naturally in this system, which should be treated separately [18]. The first are the so-called full-wave or symmetrical modes, for which the sign of $t_{ij}$ is the same for all resonator pairs $(i, j)$. In this case, we can write, in matrix notation,

$$H_I = H_s = -tA_{LG}, \qquad (3)$$

where $A_{LG}$ stands for the adjacency matrix of the corresponding line graph. The second set of modes are the half-wave or antisymmetrical modes, for which the sign of $t_{ij}$ varies throughout the lattice. The signs of $t_{ij}$ depend on a chosen

orientation of the edges of the layout graph $G$. This means that each edge of $G$ should be assigned a head vertex and a foot vertex. We can then write

$$H_I = H_a = -tA^*_{LG}, \tag{4}$$

where the matrix $A^*_{LG}$ is such that its entries are [18]

$$[A^*_{LG}]_{ij} = \begin{cases} 1, & \text{if } e_i^+ = e_j^+ \text{ or } e_i^- = e_j^-, \\ -1, & \text{if } e_i^+ = e_j^- \text{ or } e_i^- = e_j^+, \\ 0, & \text{otherwise}, \end{cases} \tag{5}$$

where $e_i^\pm$ denotes the head $(+)$ and foot $(-)$ of the oriented edge whose midpoint is $i \in L(G)$ and the comparisons in Eq. (5) refer to the vertex shared by the edges $i$ and $j$. The matrix $A^*_{LG}$ is the adjacency matrix of the so-called signed line graph of the layout (see, e.g., Ref. [29] for further details on signed graphs). Although its entries depend on the chosen orientation for $G$, a change of orientation of any edge of $G$ (a so-called switching operation) preserves the spectra of Eq. (4). Actually, a switching operation corresponds to a gauge transformation of the Hamiltonian (1), which obviously preserves the spectra. In order to see this, let us consider an edge of the layout lattice. Its midpoint is a lattice site of the line graph, which we will identify as site 0. Now perform a switching operation, i.e., change the orientation of this edge while preserving all the other edge orientations. From Eq. (5), it is easy to see that this reverses the signs of the hopping amplitudes $t_{0j}$ between site 0 and its nearest neighbors in the line graph, while leaving all the other hopping amplitudes unchanged. In other words, the only change in the tight-binding Hamiltonian is in the terms

$$\sum_{\langle 0j\rangle} t_{0j}(a_0^\dagger a_j + a_j^\dagger a_0) \to -\sum_{\langle 0j\rangle} t_{0j}(a_0^\dagger a_j + a_j^\dagger a_0). \tag{6}$$

Now, this is a particular case of a lattice gauge transformation [a more general $U(1)$ transformation would involve distinct phases $e^{i\phi_{ij}}$], which can be easily undone through the canonical transformation of the creation and annihilation operators given by $a_0 \to -a_0$, $a_0^\dagger \to -a_0^\dagger$.

## III. HIGHER-DIMENSIONAL GEOMETRIES.

Circuits based on $\{p, q\}$ tilings with $q > 3$ naturally lead to some effective higher-dimensional structures. Figure 2 depicts, for example, the $\{4, 4\}$ and $\{6, 4\}$ tilings of $\mathbb{E}^2$ [(a)] and $\mathbb{H}^2$ [(c)], and their associated line graphs [(b) and (d)], respectively. Note the higher-dimensional "cages" (tetrahedra) of the line graphs. Our proposal for the construction of these lattices depends critically on the existence of efficient implementations of symmetric planar capacitors with $q$-legs. Figure 1 depicts a possible star-shaped construction for these devices based on the usual techniques of cQED, see Appendix A for further details. In such a device, *any* pair of legs experiences the same mutual capacitance, not only adjacent ones.

In general, the quantum dynamics of a $\{p, q\}$-layout circuit will be determined by its line graph (see Fig. 2): the full and half-wave modes will be governed, respectively, by Eqs. (3) and (4). Such line graphs are composed of vertex-sharing subgraphs, each of which is a regular $(q-1)$ simplex. A regular $n$ simplex is the convex hull (polyhedron) of $n+1$ equidistant points in some $n$-dimensional space. For the $q = 4$ case of Fig. 2, this simplex is a regular tetrahedron. Note that the simplices are regular due to the symmetry of the capacitive coupling and the homogeneity of the resonators. In general, the line graph associated with a $\{p, q\}$ layout with symmetric couplings will be a regular graph with $2(q-1)$ edges per vertex, corresponding to a structure of corner-sharing identical $(q-1)$ simplices. Such structures of corner-sharing identical $n$ simplices are known in the literature as $n$-dimensional zeolites [28]. Besides, its geometrical realization as an embedding, *if possible*, clearly demands at least a $(q-1)$-dimensional background space, which cannot be Euclidean unless the original layout is also Euclidean. Again, for $q = 4$, we need 3 dimensions, as seen in Fig. 2(d).

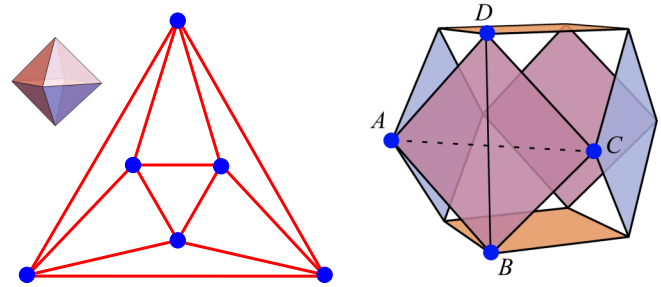


FIG. 3. The $\{3, 4\}$ tiling of $\mathbb{S}^2$. Left: the octahedron in $\mathbb{E}^3$ and its associated planar graph, which can be implemented as a circuit with symmetrical 4-leg capacitors. Right: the cuboctahedron (rectified octahedron) as a schematic representation of the the octahedron line graph, which corresponds to 6 corner-sharing tetrahedra. Each square face of the cuboctahedron is in fact a tetrahedra, but only one is depicted for simplicity. Such structure does not exist in $\mathbb{E}^3$, but can be embedded in $\mathbb{E}^5$, see the text.

It should be emphasized, however, that not all corner-sharing $(q-1)$-simplex frameworks corresponding to a $\{p, q\}$-tiling line graph will admit layered embeddings as those depicted in Fig. 2. This happens, for example, in the $\{5, 4\}$ tiling of $\mathbb{H}^2$. In this case, the presence of the pentagon odd cycles precludes the possibility of embedding the corner-sharing tetrahedra in two parallel planes as is possible for even $p$. These cases, called combinatorial zeolites, correspond to situations without clear geometrical realization, which nonetheless have proven to be interesting from a theoretical point of view [30]. Our proposal allows for such layouts to be constructed as planar circuits and their quantum dynamics to be explored.

### A. Geometrical properties of the circuits

Even though we are restricted by construction to planar circuits, and consequently to layouts corresponding to planar graphs, our $q$-leg symmetrical coupling can effectively originate quite generic higher-dimensional Kagomé-like structures. Let us consider, for the sake of illustration, the case of the octahedral graph $\{3, 4\}$, which is the simplest 4-regular planar graph with 6 vertices and 12 edges, corresponding to the $\{3, 4\}$ tiling of $\mathbb{S}^2$. The associated Kagomé structure in this case (the octahedron line graph) is clearly a nonplanar graph with 6 pairwise corner-sharing tetrahedra, see Fig. 3. However, it is easy to see that it is impossible to assemble

such structure in $\mathbb{E}^3$. We necessarily have to go to higher-dimensional spaces to get a geometrical representation of the octahedron Kagomé structure! The simplest way to embed such structure in a homogeneous space is to consider the octahedron not as embedded in $\mathbb{E}^3$, but in $\mathbb{E}^5$, the smallest Euclidean space where we can accommodate 6 equidistant points. One possible realization is to locate the vertices of the octahedron at the points (1,0,0,0,0), (0,1,0,0,0), (0,0,1,0,0), (0,0,0,1,0), (0,0,0,0,1), and $(\varphi, \varphi, \varphi, \varphi, \varphi)$, with $\varphi = \frac{1}{5}(1 \pm \sqrt{6})$, and connect them accordingly. In this way, the resulting line graph will correspond to a configuration with 6 pairwise corner-sharing tetrahedra in $\mathbb{E}^5$, which has effectively arisen from the planar circuit corresponding to the octahedral graph, as depicted in Fig. 3.

Notice that the inverse problem for these circuits is also well posed in the sense that, given, for instance, some real or hypothetical $n$-zeolite framework, one can in principle determine its equivalent planar layout. This corresponds to determining the original graph given its line graph, and such a problem is known to be well posed in general and it is indeed efficiently implemented in several graph-computing packages [31]. As an example, it is easy to see that the line graph of a star graph $S_{n+1}$ with $n+1$ leaves is the complete graph $K_{n+1}$, which denotes our $n$ simplex. Hence, one can determine the circuit equivalent to a certain $n$-zeolite framework substituting the $n$- simplexes with star graphs $S_{n+1}$ and connecting the vertices accordingly. This can be illustrated with the octahedron case of Fig. 3. It is not difficult to get the original circuits from the corner-sharing $n$-simplex framework by replacing the $n$-simplexes by $S_{n+1}$ graphs.

Finally, we stress that since we are restricted to planar layouts, the corresponding graph circuits will always be embedded in a two-dimensional manifold. In particular, the continuous limit of Ref. [18] in our case will also give origin to two-dimensional geometries. However, due to the design flexibility of our $q$-leg capacitor, we can explore layouts with spatially varying coordination $q$, which could simulate a nonuniform curvature in a two-dimensional space and, consequently, expand the results of Ref. [18] to nonuniform geometries.

### B. Positive-curvature lattices

It is worth mentioning that even circuits with $q = 3$, as those originally considered in Ref. [17], can also give rise to effectively higher-dimensional structures. This is the case, for example, of the fullerenes discussed in Ref. [18]. These correspond to lattices with positive curvature, tilings of the two-sphere $\mathbb{S}^2$, whose embedding requires 3 dimensions. However, both the $C_{60}$ and $C_{84}$ finite tilings of $\mathbb{S}^2$ considered in Ref. [18] involve two different types of faces: pentagons and hexagons. Hence, the associated Kagomé decoration will necessarily also involve some isosceles triangles besides the equilateral ones associated with the symmetrical capacitor. Although our star-shaped proposal for the capacitor is also able to emulate the isosceles triangles of the associated line graph, one can circumvent this problem by considering the regular dodecahedron circuit shown in Fig. 4, which can be viewed as the $\{5, 3\}$ tiling of the sphere $\mathbb{S}^2$. Since any spherical tiling admits a planar representation, the dodecahedron

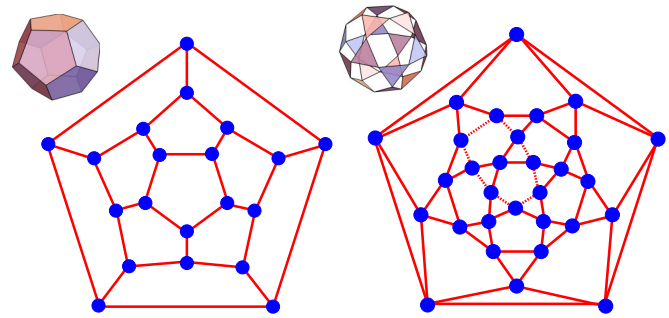

FIG. 4. A $\{5, 3\}$ tiling of $\mathbb{S}^2$. Left: the dodecahedron in $\mathbb{E}^3$ and its planar graph, which can be implemented as a circuit with symmetrical 3-leg capacitors. Right: the associated line graph, which is realized as the triangular faces of an icosidodecahedron in $\mathbb{E}^3$, and its respective 30-vertex graph. The dashed line corresponds to one of the ten even cycles associated with the flat band in the spectra of the icosidodecahedron graph.

can be realized as a planar layout circuit, as also shown in Fig. 4. Its line graph is a finite Kagomé lattice known as an icosidodecahedron (the rectified dodecahedron), a well-known Archimedean solid. This is quite an interesting case to be explored as a circuit due to its amenable size and known analytical spectra.

## IV. SOME EXACT RESULTS ABOUT THE SPECTRA

All the analyses and experiments of Ref. [17], which we propose to extend here, require the knowledge of the excitation spectra of the Hamiltonian of Eq. (1) for both full- and half-wave modes. For this, some classical results for finite graphs prove useful. In particular, Lemma 2.1 of Ref. [32] applied to $A_{LG}$ reads

$$\chi(A_{LG}, \lambda) = (\lambda + 2)^{m-n} \chi(Q, \lambda + 2), \tag{7}$$

where $\chi(M, \lambda)$ denotes the characteristic polynomial for the matrix $M$ in the variable $\lambda$, and $Q = D + A$, with $D$, $A$, $n$, and $m$ standing for the degree matrix, the adjacency matrix, the number of vertice,s and the number of edges of the *layout* $G$, respectively. The degree of a graph vertex is the number of edges connecting to it (coordination number), and hence the degree matrix here is the diagonal matrix whose entries correspond to the number of resonators connected to each capacitor in the layout circuit. The matrix $Q$ is known in the graph literature as the signless Laplacian matrix of the graph $G$ (see, e.g., Ref. [33]). The same Lemma applied to $A^*_{LG}$ gives

$$\chi(A^*_{LG}, \lambda) = (\lambda + 2)^{m-n} \chi(L, \lambda + 2), \tag{8}$$

where $L = D - A$ is the usual Laplacian matrix of the *layout* $G$. Note how Eqs. (7) and (8) relate the spectrum of the line graph $L(G)$ to properties of its layout $G$. Both matrices $Q$ and $L$ are positive semidefinite and, thus, the spectra of both $A_{LG}$ and $A^*_{LG}$ are bounded from below by $-2$. Moreover, there are flat bands with at least $m - n$ eigenvectors with eigenvalue $\lambda_{\min} = -2$ for any layout $G$. In fact, for the half-wave modes, the flat band has $m - n + 1$ eigenstates, since $L$ always has a single zero eigenvalue due to the fact that the layout is connected [32]. Furthermore, $Q$ also has one vanishing eigenvalue if and only if $G$ is bipartite, in which case we also have

$\chi(Q,\lambda) = \chi(L,\lambda)$ [33], so that $A_{LG}$ and $A^*_{LG}$ have the same spectra. This case corresponds to a layout with a balanced [29] signed line graph. Physically, this is a consequence of the fact that the two Hamiltonians corresponding to Eqs. (3) and (4) are gauge equivalent in this case. It is clear from Eqs. (7) and (8) that the spectra of the layout matrices $Q$ and $L$ suffice to determine the complete spectra of the physical Hamiltonian of Eq. (1) for both full- and half-wave modes. All the other eigenvalues belong to the flat band at $\lambda = -2$.

Let us illustrate this with the finite $\{5,3\}$ tiling of $\mathbb{S}^2$ of Fig. 4, whose associated line graph is the icosidodecahedron. The layout in this case has $L = 3I - A$ and $Q = 3I + A$. Moreover, for the dodecahedron [33]

$$\chi(A,\lambda) = (\lambda-3)(\lambda^2-5)^3(\lambda-1)^5\lambda^4(\lambda+2)^4, \quad (9)$$

and from Eqs. (7) and (8), we have finally the icosidodecahedral graph spectra

$$S(A_{LG}) = \{-2_{10}, (1-\sqrt{5})_3, -1_4, 1_4, 2_5, (1+\sqrt{5})_3, 4_1\}, \quad (10)$$

$$S(A^*_{LG}) = \{-2_{11}, (1-\sqrt{5})_3, 0_5, 1_4, (1+\sqrt{5})_3, 3_4\}, \quad (11)$$

where the indices give the respective eigenvalue multiplicities. One can see that the flat band, which corresponds roughly to 1/3 of the total spectra, effectively comes from the $m - n = 10$ term in Eqs. (7) and (8). For the full-wave modes, it is quite easy to identify the flat-band eigenvectors: they correspond to an alternating sequence of 1 and $-1$ along even cycles as the one depicted in Fig. 4, and zero elsewhere [18]. These cycles are closed paths that go through a unique edge of each visited triangle in the line graph. There are 10 linearly independent even cycles of this type in the icosidodecahedron graph, and hence an equal number of $-2$ eigenvalues of $A_{LG}$. Finally, since we are dealing with a regular graph, the largest eigenvalue of $A_{LG}$ is precisely the line-graph degree, see the Appendix B.

### Flat fraction of the spectra

For a large $\{p,q\}$ layout, the fraction $f = \frac{m-n}{m}$ $(m \gg 1)$ of the spectra corresponding to the flat band is an important property of the circuit. We can determine $f$ from the growth properties of the layout graphs (see Appendix B for further details). For large hyperbolic layouts, the flat-band fraction tends *exponentially* to

$$f = \frac{q-2}{\sigma - 1 + q}, \quad (12)$$

where

$$\sigma = \frac{\tau - 2 + \sqrt{\tau^2 - 4\tau}}{2}, \quad (13)$$

with $\tau$ given by Eq. (2). For hyperbolic tilings, $\sigma > 1$. Equation (12) is also valid for Euclidean tilings (for which $\sigma = 1$) but the convergence is a power law. Spherical tilings are finite and this discussion does not apply. For the sake of illustration, Fig. 5 depicts the spectra for some $\{p,q\}$ layouts. Such spectra are key ingredients in the kinds of experiments performed in Ref. [17] and which we propose to extend to $q > 3$ configurations.

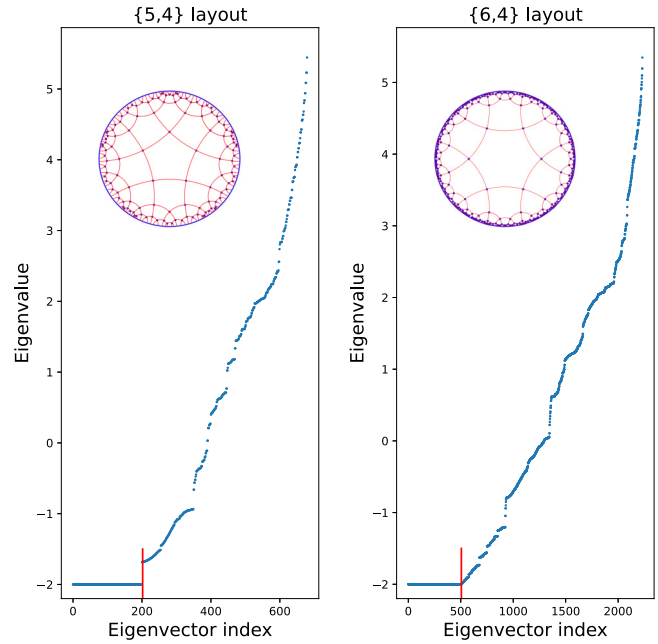


FIG. 5. Spectra of the line-graph adjacency matrix $A_{LG}$ for some $\{p,q\}$ layouts, with the red vertical line highlighting the predicted flat-band endpoint. Left: a layout of 4 concentric rings of the $\{5,4\}$ hyperbolic tilling. The associated line graph has 681 vertices. The predicted flat-band fraction is $f = 0.297$. Note the gap between the flat band and the rest of the spectra, a property of all layouts with odd $p$. Since $p = 5$, this circuit cannot be interpreted as a layer of corner-sharing tetrahedra as in Fig. 2. Right: a layout of 4 concentric rings of the $\{6,4\}$ hyperbolic tilling of Fig. 2. The associated line graph has 2233 vertices. The predicted flat-band fraction is $f = 0.226$. For even $p$, there is no gap between the flat band and the rest of the spectra.

## V. CONCLUSIONS

In summary, we have shown that, with present-day technology, planar circuit quantum electrodynamics can be explored to simulate some higher-dimensional Euclidean and non-Euclidean structures as, e.g., some $n$-dimensional zeolites, opening the doors to a myriad of new possibilities in metamaterial studies and other related fields. We have investigated the spectral properties of line graphs associated with polygon-centered $\{p,q\}$ layouts, with special emphasis on hyperbolic geometries. Using an exact recurrence relation governing the layered growth of these layouts, we derived the flat-band fraction $f_\ell$ and established its exponential convergence to a finite value in hyperbolic tilings, in contrast with the algebraic convergence observed in Euclidean cases. These results provide a precise characterization of the asymptotic spectral weight of the flat band as a function of the local curvature encoded by $p$ and $q$. We also analyzed the deviation of the average degree $\langle k \rangle$ from the regular value $q$ in finite layouts, showing that the degree deficit is concentrated at the boundary and persists regardless of system size due to the exponential growth of hyperbolic structures. This effect ensures the presence of undercoordinated vertices even in large systems and reinforces the robustness of the flat band.

Finally, motivated by these theoretical insights, we are currently developing superconducting circuits based on compact hyperbolic layouts, notably a dodecahedral configuration. More specifically, we are exploring microwave-guide circuits constructed with sputtered niobium films on silicon substrates. This architecture is designed to probe the spectral features discussed here and to explore experimentally the interplay between geometric frustration, flat-band localization, and nontrivial connectivity. A detailed report on this ongoing work will be provided in a future publication [34]. Additionally, another promising avenue for exploration is the study of lattices with spatially varying coordination $q$, which can simulate nonuniform curvature.

## ACKNOWLEDGMENTS

The authors acknowledge the financial support of the National Council for Scientific and Technological Development (CNPq, Brazil) through Grants No. 302674/2018-7 (A.S.) and No. 309584/2021-3 (E.M.), the São Paulo Research Foundation (FAPESP, Brazil) through Grants No. 2017/08602-0, No. 2017/22037-4, and No. 2017/22035-1 (F.R.).

## DATA AVAILABILITY

The data that support the findings of this article are not publicly available. The data are available from the authors upon reasonable request.

## APPENDIX A: THE $q$-leg SYMMETRIC CAPACITOR

We now discuss an efficient implementation of a symmetric planar capacitor with $q$ legs, essential for the cQED application we are proposing. Figure 1 illustrates the schematic geometry of devices featuring 4 and 5 legs. The $q$-leg coupling element, designed as a single central star-shaped section with $q$ legs, is positioned at the convergence point of the microwave cavities. Each of these cavities is formed from a segment of a $Z_0 = 50\ \Omega$ planar transmission line, coupled at its rf input and output ports through small capacitors $C_{\text{legs}}$. These capacitors set the boundary conditions of the cavity as voltage antinodes, facilitating standing-wave resonances with wavelengths $\lambda = 2L/n$, where $L$ is the cavity length and $n$ is an integer. These components can be manufactured using standard microfabrication techniques in a single-layer device.

In the weak-coupling limit, where the coupling capacitors $C_{\text{legs}}$, connecting the transmission-line resonators to the $q$-leg coupling element, are small compared to the total capacitance of the resonator $C_R$, the $q$-leg elements can be adiabatically eliminated [14,15], allowing the system to be effectively described by a tight-binding Hamiltonian, as shown in Eq. (1). The photon-hopping amplitude between two resonators is then [14,15]

$$t_{ij} \propto C_{\text{legs}}\phi_{ij}, \tag{A1}$$

where $\Phi_{ij}$ is the voltage-mode function of the pair $(i, j)$.

To ensure homogeneous photon-hopping amplitudes, the capacitance between any two resonators $(i, j)$ within the network must be the same. To demonstrate the viability of constructing such devices, we simulated the capacitance between the cavities depicted in Fig. 1 using the Ansys Q3D Extractor software. This process involved utilizing the CAD file of our circuit to solve Maxwell's equations, thereby determining the field and charge distributions. Employing standard parameters used in cQED devices, we conducted electrostatic simulations of the $q$-leg geometry based on the layout illustrated in Fig. 1. These simulations were performed for devices on a 500 μm silicon substrate with a relative permittivity of 11.45, and the superconducting thin film was modeled as a 100-nm thick perfect electric conductor. The resulting capacitance between any two legs was determined to be $0.37399 \pm 0.00001$ fF and $0.27110 \pm 0.00003$ fF for the 4-leg and 5-leg configurations, respectively. These results suggest that the proposed geometry for the $q$-leg capacitor can achieve uniform photon hopping within the circuit.

## APPENDIX B: SPECTRA AND GROWTH PROPERTIES OF LAYOUTS

The fraction $f = \frac{m-n}{m}$ corresponding to the proportion of zero eigenvalues in the spectrum of the adjacency matrix of the line graph, which corresponds to the flat band, is a key feature in the spectral analysis of these circuits. Recalling that the average degree $\langle k\rangle$ of a graph with $m$ edges and $n$ vertex is given by

$$\langle k\rangle = \frac{2m}{n}, \tag{B1}$$

we have

$$f = 1 - \frac{2}{\langle k\rangle}. \tag{B2}$$

We can obtain the fraction $f$ for finite $\{p, q\}$-hyperbolic layouts from the growth properties of these graphs. The problem of the growth of vertex-centered hyperbolic tilings was considered in Ref. [35]. One can easily adapt that approach to our problem of growing polygon-centered layouts by the accretion of concentric layers of tilings. Let us assume we have a layout composed of $\ell$ concentric rings of vertices, ordered outwards, of a $\{p, q\}$ tiling, with $p > 3$. It will become clear that the case of a triangular tiling ($p = 3$) is intrinsically different and will not be treated here since it does not seem to be interesting for our purposes. Each ring $j$ contains two types of vertices: type-$B$ vertices, which connect to the previous $(j-1)$th ring, and type-$b$ vertices, which do not. These are illustrated in Fig. 6. Let $b_j$ be the number of vertices on the $j$ th ring that are not connected to the $(j-1)$ th one, and $B_j$ the number of remaining vertices which are connected to previous ring. For example, for the $\{6, 4\}$ tiling of Fig. 2, one has $b_1 = 6$, $B_1 = 0$, $b_2 = 30$, $B_2 = 12$, and so on. Each edge emanating from the $j$ th ring will necessarily reach a $B$-type vertex in the $(j+1)$ th ring and, thus, we have

$$B_{j+1} = (q-2)b_j + (q-3)B_j. \tag{B3}$$

The recurrence for the $b$ vertices is a little more intricate. From Fig. 6, we see that for each $B$ vertex, there are $q-2$ polygons between the $j$ th and the $(j+1)$ th rings. For the $b$ vertices, there are $q-1$ of such polygons. Each one of these polygons, which we assume to be ordered anticlockwise, will lead to $p-3$ $b$ vertices in the $(j+1)$ th ring. To compute $b_{j+1}$, we

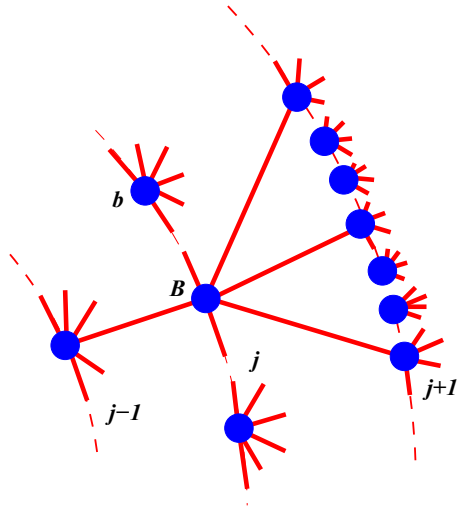


FIG. 6. Three concentric rings of a polygon-centered $\{p, q\}$ layout ($p > 3$) with their two types of vertices: the $B$ type, connecting the $j$ th ring to the previous $(j-1)$ th one, and the $b$ type, that do not connect to the previous ring. There are $q$ edges meeting at every vertex.

run circularly over all these polygons between the $j$ th and the $(j+1)$ th rings. In order to avoid double counting, we neglect the last polygon of each vertex, since it coincides with the first one of the next vertex. We must also neglect one vertex in the sum of each vertex in the $j$ th, since the first polygon, in contrast to the other ones (with the exception of the last), has one of its edges on the $j$ th ring. Finally, we have the following recurrence system, valid for $p > 3$,

$$\begin{pmatrix} b_{j+1} \\ B_{j+1} \end{pmatrix} = \begin{pmatrix} (q-2)(p-3)-1 & (q-3)(p-3)-1 \\ q-2 & q-3 \end{pmatrix} \times \begin{pmatrix} b_j \\ B_j \end{pmatrix}. \tag{B4}$$

For any polygon-centered $\{p, q\}$ layout, the initial condition for Eq. (B4) is $b_1 = p$ and $B_1 = 0$. We can determine the number of edges $m_\ell$ and vertices $n_\ell$ of a $\{p, q\}$ layout consisting of $\ell$ concentric rings from the function $B_\ell$ alone. Following Ref. [35], let $t_\ell$ be the number of polygons in the layout. Then,

$$t_\ell = 1 + \sum_{j=1}^{\ell} B_j. \tag{B5}$$

The number of vertices in the same layout will be given by

$$n_\ell = \sum_{j=1}^{\ell} (b_j + B_j) = \frac{1}{q-2} \sum_{j=1}^{\ell} (B_{j+1} + B_j) = \frac{B_{\ell+1} + 2(t_\ell - 1)}{q-2}, \tag{B6}$$

where Eq. (B3) was used. The number of edges $m_\ell$ can be determined from Euler's formula for planar graphs

$$n_\ell - m_\ell + t_\ell = 1, \tag{B7}$$

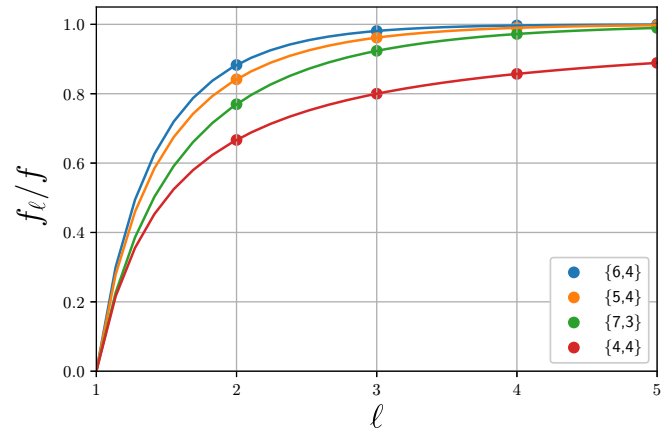


FIG. 7. Convergence of $f_\ell / f$ as a function of the number of rings $\ell$ of the layout [see Eqs. (12) and (B8)] for different tilings. The convergence for hyperbolic tilings is exponential, in contrast to the power-law convergence for the Euclidean case ($\{4, 4\}$).

from which we finally have the fraction

$$f_\ell = \frac{m_\ell - n_\ell}{m_\ell} = \frac{q-2}{C_\ell + q}, \tag{B8}$$

where

$$C_\ell = \frac{B_{\ell+1}}{t_\ell - 1}. \tag{B9}$$

The fraction of Eq. (B8) for large layouts is determined by $\lim_{\ell\to\infty} C_\ell$. In order to evaluate this limit, let us consider the equation for $B_\ell$ obtained from the recurrence system of Eq. (B4)

$$B_{\ell+1} = (\tau - 2)B_\ell - B_{\ell-1}, \tag{B10}$$

with $\tau$ given by Eq. (2), whose solution for our case is

$$B_\ell = \frac{p(q-2)}{\sigma^2 - 1}(\sigma^\ell - \sigma^{2-\ell}), \tag{B11}$$

with $\sigma$ given by Eq. (13). Note that this solution is valid only for hyperbolic tilings. For Euclidean ones $\sigma = 1$ and the solution is $B_\ell = p(q-2)(\ell - 1)$. From Eq. (B11),

$$t_\ell = 1 + \frac{p(q-2)}{\sigma^2 - 1} \frac{\sigma^{\ell+1} - \sigma^2 - \sigma + \sigma^{2-\ell}}{\sigma - 1}, \tag{B12}$$

yielding

$$C_\ell = \frac{(\sigma - 1)(1 - \sigma^{-2\ell})}{1 + \sigma^{1-2\ell} - (\sigma + 1)\sigma^{-\ell}}, \tag{B13}$$

and finally

$$\lim_{\ell\to\infty} C_\ell = \sigma - 1, \tag{B14}$$

from which Eq. (12) follows immediately. For Euclidean tilings, we have instead

$$C_\ell = \frac{2}{\ell - 1}, \tag{B15}$$

which is also compatible with Eq. (12), albeit with a slower power-law convergence. Figure 7 illustrates the convergence of $f_\ell$ as a function of the number of rings $\ell$ of the layout for different tilings.

It is worth mentioning that from Eqs. (12) and (B2), the average degree of a large $\{p, q\}$ layout is

$$\langle k\rangle = 2\left(\frac{\sigma - 1 + q}{\sigma + 1}\right). \tag{B16}$$

This shows that, although hyperbolic tilings are $q$ regular, we always have $\langle k\rangle < q$ for any finite hyperbolic layout, no matter how large it is. This is hardly surprising since all vertices with degree deficiency ($k < q$) are located in the outermost ring of the layout and hyperbolic tilings grow exponentially. In contrast, Euclidean tilings grow linearly and have $\langle k\rangle = q$.

Besides the flat band, we can also estimate the largest eigenvalues of $A_{LG}$ and $A^*_{LG}$ from some classical results for the spectra of the matrices $Q$ and $L$. For instance, if $\mu$ stands for the largest eigenvalue of $Q$, one has [33] $2k_{\min} \leqslant \mu \leqslant 2k_{\max}$, where $k_{\min}$ and $k_{\max}$ stand for, respectively, the minimal and maximal degree of the layout, with the equality holding if and only if $G$ is regular. For our case, $k_{\min} = 2$ in the outermost ring and $k_{\max} = q$, implying

$$2 \leqslant \max[S(A_{LG})] \leqslant 2(q - 1). \tag{B17}$$

There are many similar bounds for the largest eigenvalue of the Laplacian matrix, and they can be used to estimate the largest eigenvalues of $A^*_{LG}$ analogously. For instance, from the elementary bound [32] $k_{\max} \leqslant \nu \leqslant 2k_{\max}$ for the the largest eigenvalue $\nu$ of $L$, we have

$$q - 2 \leqslant \max[S(A^*_{LG})] \leqslant 2(q - 1). \tag{B18}$$

These bounds can be checked against Fig. 5.


[1] M. Atiyah, R. Dijkgraaf, and N. Hitchin, Geometry and physics, Philos. Trans. R. Soc. A **368**, 913 (2010).

[2] J. Steinhauer, Observation of quantum Hawking radiation and its entanglement in an analog black hole, Nat. Phys. **12**, 959 (2016).

[3] S. Eckel, A. Kumar, T. Jacobson, I. B. Spielman, and G. K. Campbell, A rapidly expanding Bose-Einstein condensate: An expanding universe in the lab, Phys. Rev. X **8**, 021021 (2018).

[4] V. I. Kolobov, K. Golubkov, J. R. Muñoz de Nova, and J. Steinhauer, Observation of stationary spontaneous Hawking radiation and the time evolution of an analog black hole, Nat. Phys. **17**, 362 (2021).

[5] T. G. Philbin, C. Kuklewicz, S. Robertson, S. Hill, F. König, and U. Leonhardt, Fiber-optical analog of the event horizon, Science **319**, 1367 (2008).

[6] S. Weinfurtner, E. W. Tedford, M. C. Penrice, W. G. Unruh, and G. A. Lawrence, Measurement of stimulated Hawking emission in an analog system, Phys. Rev. Lett. **106**, 021302 (2011).

[7] G. Tarjus, S. A. Kivelson, Z. Nussinov, and P. Viot, Frustration-based approach of supercooled liquids and the glass transition: a review and critical assessment, J. Phys.: Condens. Matter **17**, R1143 (2005).

[8] C. G. Callan and F. Wilczek, Infrared behavior at finite temperature, Nucl. Phys. B **340**, 366 (1990).

[9] J. Maldacena, The large-$N$ limit of superconformal field theories and supergravity, Int. J. Theor. Phys. **38**, 1113 (1999).

[10] R. Krcmar, T. Iharagi, A. Gendiar, and T. Nishino, Tricritical properties of the Blume-Capel model on a square lattice in hyperbolic geometry, Phys. Rev. E **78**, 061119 (2008).

[11] K. Mnasri, B. Jeevanesan, and J. Schmalian, Critical phenomena in hyperbolic space, Phys. Rev. B **92**, 134423 (2015).

[12] N. P. Breuckmann, B. Placke, and A. Roy, Critical properties of the Ising model in hyperbolic space, Phys. Rev. E **101**, 022124 (2020).

[13] N. P. Breuckmann and B. M. Terhal, Constructions and noise thresholds of hyperbolic surface codes, IEEE Trans. Inf. Theory **62**, 3731 (2016).

[14] J. Koch, A. A. Houck, K. L. Hur, and S. M. Girvin, Time-reversal-symmetry breaking in circuit-QED-based photon lattices, Phys. Rev. A **82**, 043811 (2010).

[15] A. Nunnenkamp, J. Koch, and S. M. Girvin, Synthetic gauge fields and homodyne transmission in Jaynes-Cummings lattices, New J. Phys. **13**, 095008 (2011).

[16] A. Blais, S. M. Girvin, and W. D. Oliver, Circuit QED in the ultra-strong coupling regime, Nat. Phys. **16**, 247 (2020).

[17] A. J. Kollar, M. Fitzpatrick, and A. A. Houck, Hyperbolic lattices in circuit quantum electrodynamics, Nature (London) **571**, 45 (2019).

[18] A. J. Kollar, M. Fitzpatrick, P. Sarnak, and A. A. Houck, Line-graph lattices for hyperbolic band theory, Commun. Math. Phys. **376**, 1909 (2020).

[19] I. Boettcher, P. Bienias, R. Belyansky, A. J. Kollar, and A. V. Gorshkov, Quantum simulation of hyperbolic space with circuit quantum electrodynamics: From dimensions to fractons, Phys. Rev. A **102**, 032208 (2020).

[20] J. Maciejko and S. Rayan, Hyperbolic band theory, Sci. Adv. **7**, eabe9170 (2021).

[21] S. Yu, X. Piao, and N. Park, Topological photonic states in hyperbolic lattices, Phys. Rev. Lett. **125**, 053901 (2020).

[22] A. A. Houck, H. E. Türeci, and J. Koch, On-chip quantum simulation with superconducting circuits, Nat. Phys. **8**, 292 (2012).

[23] X. Zhu, J. Guo, N. P. Breuckmann, H. Guo, and S. Feng, Hyperbolic circuits for strongly correlated quantum matter, J. Phys.: Condens. Matter **33**, 335602 (2021).

[24] M. V. W. Fitzpatrick, Lattices in circuit quantum electrodynamics: A platform for nonequilibrium quantum simulation, Ph.D. thesis, Princeton University, 2019.

[25] M. Scigliuzzo, G. Calajò, F. Ciccarello, D. P. Lozano, A. Bengtsson, P. Scarlino, A. Wallraff, D. Chang, P. Delsing, and S. Gasparinetti, Extensible quantum simulation architecture based on atom-photon bound states in an array of high-impedance resonators, Phys. Rev. X **12**, 031036 (2022).

[26] X. Zhang, E. Kim, D. K. Mark, S. Choi, and O. Painter, A superconducting quantum simulator based on a photonic-bandgap metamaterial, Science **379**, 278 (2023).

[27] K. O'Brien, M. Amouzegar, W. Lee, M. Ritter, and A. Kollar, A circuit-QED lattice system with flexible connectivity

and gapped flat bands for photon-mediated spin models, arXiv:2505.05559.

[28] D. Bonchev and D. H. Rouvray, *Chemical Topology: Applications and Techniques* (Gordon and Breach Science Publishers, The Netherlands, 2000).

[29] T. Zaslavsky, Signed graphs, Discrete Appl. Math. **4**, 47 (1982).

[30] T. Jordan, II–combinatorial rigidity: Graphs and matroids in the theory of rigid frameworks, MSJ Mem. **34**, 33 (2016).

[31] A. A. Hagberg, D. A. Schult, and P. J. Swart, in *Proceedings of the 7th Python in Science Conference (SciPy2008)*, edited by G. Varoquaux, T. Vaught, and J. Millman (Pasadena, CA, 2008), pp. 11–15.

[32] D. M. Cvetković, M. Doob, and H. Sachs, *Spectra of Graphs: Theory and Application* (Academic Press, London, 1980).

[33] D. Cvetkovic, P. Rowlinson, and S. K. Simić, Signless Laplacians of finite graphs, Linear Algebra Appl. **423**, 155 (2007).

[34] E. Cunha, L. M. Ruela, D. D. C. Brito, E. Miranda, A. Saa, and F. Rouxinol, Exploring non-Euclidean lattices and flat bands in a dodecahedral network using circuit quantum electrodynamics (unpublished).

[35] J. F. Moran, Growth in graphs, the structure of certain subgroups and their lattice quotients, Discrete Math. **173**, 151 (1997).